

Tuning Nanoparticle Interactions with Ovarian Cancer through Layer-by-Layer Modification of Surface Chemistry

Santiago Correa, Natalie Boehnke, Antonio E. Barberio, Elad Deiss-Yehiely, Aria Shi, Benjamin Oberlton, Sean G. Smith, Ioannis Zervantonakis, Erik C. Dreaden, and Paula T. Hammond*

Cite This: *ACS Nano* 2020, 14, 2224–2237

Read Online

ACCESS |

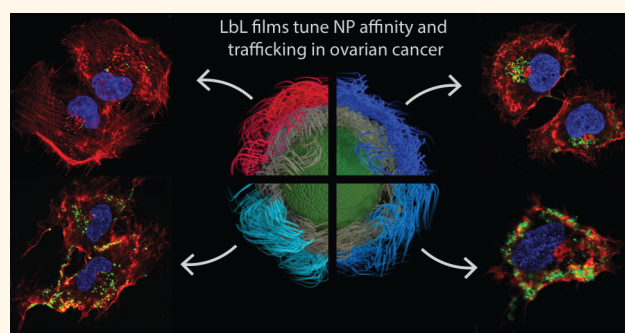
Metrics & More

Article Recommendations

Supporting Information

ABSTRACT: Nanoparticle surface chemistry is a fundamental engineering parameter that governs tumor-targeting activity. Electrostatic assembly generates controlled polyelectrolyte complexes through the process of adsorption and charge overcompensation utilizing synthetic polyions and natural biomacromolecules; it can yield films with distinctive hydration, charge, and presentation of functional groups. Here, we used electrostatic layer-by-layer (LbL) assembly to screen 10 different surface chemistries for their ability to preferentially target human ovarian cancer *in vitro*. Our screen identified that poly-L-aspartate, poly-L-glutamate, and hyaluronate-coated LbL nanoparticles have striking specificity for ovarian cancer, while sulfated poly(β -cyclodextrin) nanoparticles target noncancerous stromal cells. We validated top candidates for tumor-homing ability with a murine model of metastatic disease and with patient-derived ovarian cancer spheroids. Nanoparticle surface chemistry also influenced subcellular trafficking, indicating strategies to target the cell membrane, caveolae, and perinuclear vesicles. Our results confirm LbL is a powerful tool to systematically engineer nanoparticles and achieve specific targeting.

KEYWORDS: nanomedicine, tumor-targeting, surface chemistry, layer-by-layer, subcellular targeting, nanoparticles, ovarian cancer



Nanoparticle (NP) surface chemistry governs critical interactions at the nano–bio interface that determine NP pharmacokinetics and tumor-targeting.¹ To negotiate these complex interactions, translational nanomedicine has focused on antifouling surface chemistries,^{2–5} which prolong circulation to reap the most benefit from size-based, passive tumor-targeting mechanisms (*e.g.*, putative enhanced permeability and retention (EPR) effects).^{6,7} While NPs that rely on the EPR effect accumulate in murine tumors, they have failed to achieve similar tumor-targeting in humans, which has limited the clinical impact of nanomedicine.^{8,9} Likewise, active targeting strategies (*e.g.*, covalent attachment of high-affinity ligands to the NP surface to mediate endo- or transcytosis)¹⁰ have led to limited improvements in drug delivery: 1.5-fold on average.¹¹ We hypothesized that useful structure–activity relationships could be determined to guide the design of next-generation NPs by expanding the focus from traditional antifouling or ligand chemistries to examine the broad range of functional surfaces that might be derived from electrostatic assemblies formed from diverse native or synthetic polyelectrolyte chemistries.

Here, we experimentally screen a small library of surface chemistries—including polypeptides, native polysaccharides, and synthetic polymers—to elucidate how NP surface chemistry influences targeting to ovarian cancer *in vitro* and *in vivo*. We utilize the layer-by-layer (LbL) self-assembly platform, which allows traditional colloidal substrates to be functionalized with multilayered, nanoscale polymeric films through sequential adsorption of polyelectrolytes bearing alternating charges.^{12–14} As a result, LbL assembly is able to incorporate materials of significant chemical complexity, including polysaccharides and polypeptides, without the need to develop correspondingly complex and often differing chemical conjugation techniques. LbL thin films consist of an interpenetrated network of positively and negatively charged polyions, with the degree of interpenetration dependent on several factors, including the

Received: November 20, 2019

Accepted: January 23, 2020

Published: January 23, 2020

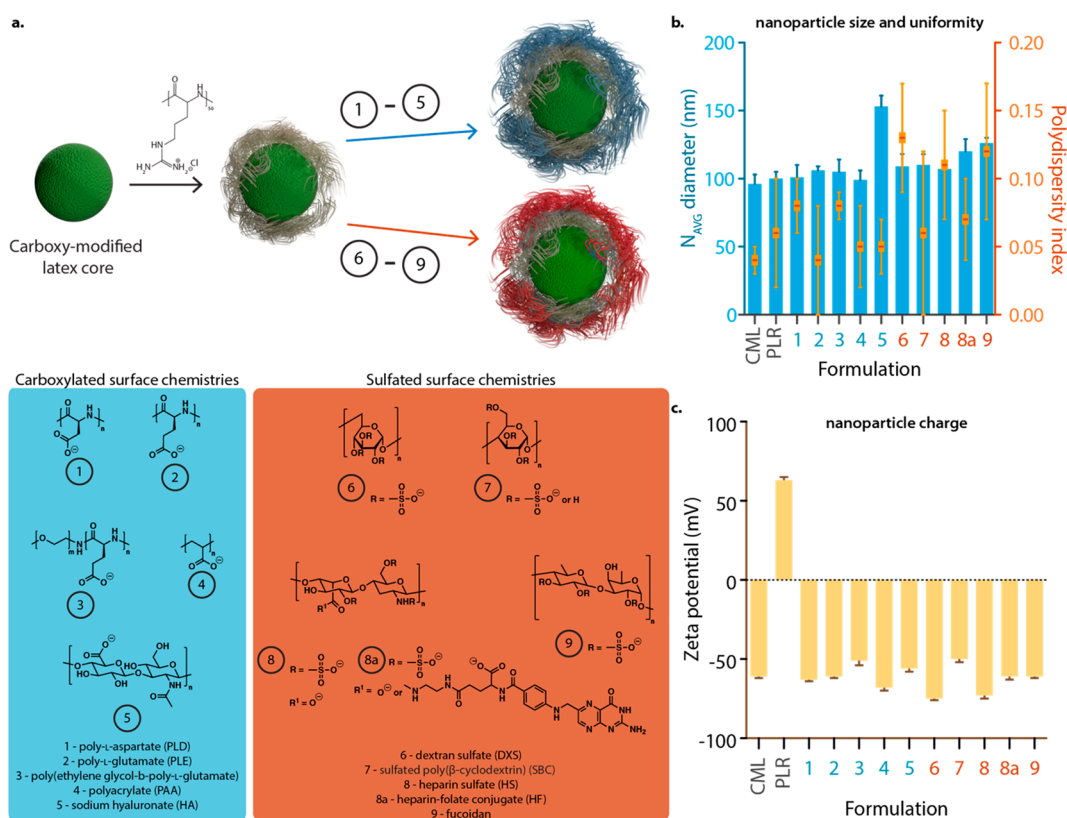


Figure 1. Layer-by-layer (LbL) modification was used to develop a panel of nanoparticles exploring diverse anionic surface chemistries. (a) Scheme of LbL functionalization; 100 nm cores were coated with poly-L-arginine followed by one of 10 different anionic polymers. (b) Size and polydispersity data were acquired by dynamic light scattering, and (c) zeta potential data were measured using laser Doppler electrophoresis. Error bars represent standard deviation of three technical replicates.

charge density of the substrate and the number of deposited layers. The outermost layer of these systems exhibits an excess of charged polymer chains that can take on a dense, loopy molecular conformation to achieve a hydrated, charged, and sterically repulsive outer shell, properties needed for systemic delivery and extended NP plasma half-lives.¹⁵ Recently, we developed an approach that substantially improved the scale and throughput of LbL-NP assembly, making it possible to screen many more formulations than was previously feasible.¹⁶

Our screen focused on high-grade serous ovarian cancer (HGSOC) because its specific metastatic progression presents challenges for efficient drug delivery. In HGSOC, small tumor nodules and spheroids disseminate widely through the intraperitoneal (IP) cavity but rarely outside of it, leading to a compartmentalized malignancy that is nonetheless difficult to drug through standard routes^{17,18} due to the relatively short half-lives of small molecules in the IP cavity and the limited tissue binding and penetration observed with PEGylated nanoparticles. By using flow cytometry to screen NP–cell binding, we found that LbL-NPs with certain carboxylated surface chemistries possess a high affinity to HGSOC cell lines and patient-derived xenograft (PDX) spheroids *in vitro*. We further validated our *in vitro* findings *in vivo* using NP screen hits in a metastatic orthotopic model of HGSOC, which confirmed that three different types of highly carboxylated LbL NPs selectively and preferentially accumulated in HGSOC tumors, yet introduced starkly different intracellular trafficking, indicating a promising avenue for future nanomedicine development.

RESULTS AND DISCUSSION

Generating a Panel of Diverse NP Surface Chemistries.

LbL-NPs were prepared with different surface chemistries that included polypeptides, native polysaccharides, and synthetic polymers. Anionic chemistries were chosen for their improved biocompatibility and systemic circulation relative to cationic NPs.^{19,20} Fluorescent 100 nm carboxy-modified latex (CML)-NPs were first coated with poly-L-arginine (PLR) and then coated with one of several polyanions bearing either sulfated (SO_3) or carboxylated (COOH) functional groups (Figure 1a). For the outermost coatings, we chose COOH and SO_3 polymers with known ligand–receptor interactions (e.g., sodium hyaluronate²¹ (HA), heparin sulfate²² (HS), and heparin-folate conjugate²³ (HF)), as well as those without known interactions (e.g., the closely related homo poly-L-amino acids poly-L-aspartate (PLD) and poly-L-glutamate (PLE)). All LbL-NPs had average hydrodynamic diameters from 100 to 155 nm, average polydispersity indices (PDI) between 0.04 and 0.13 (Figure 1b), and zeta potentials < -30 mV (Figure 1c) as measured by dynamic light scattering (DLS). Consistent with our prior work, HA-coated NPs form larger nanoparticles for two reasons. First, HA molecules form intra- and intermolecular hydrogen bonds that contribute to a thicker polymer shell. Second, HA is a highly hydrophilic polysaccharide that induces the formation of a water shell, contributing to the hydrodynamic radius measured by DLS. Transmission electron microscopy confirmed LbL-NPs were uniform and within the size ranges measured by DLS (Figure S1). For clarity, in the following text we refer to LbL-NPs by their terminal coating alone (e.g., X/

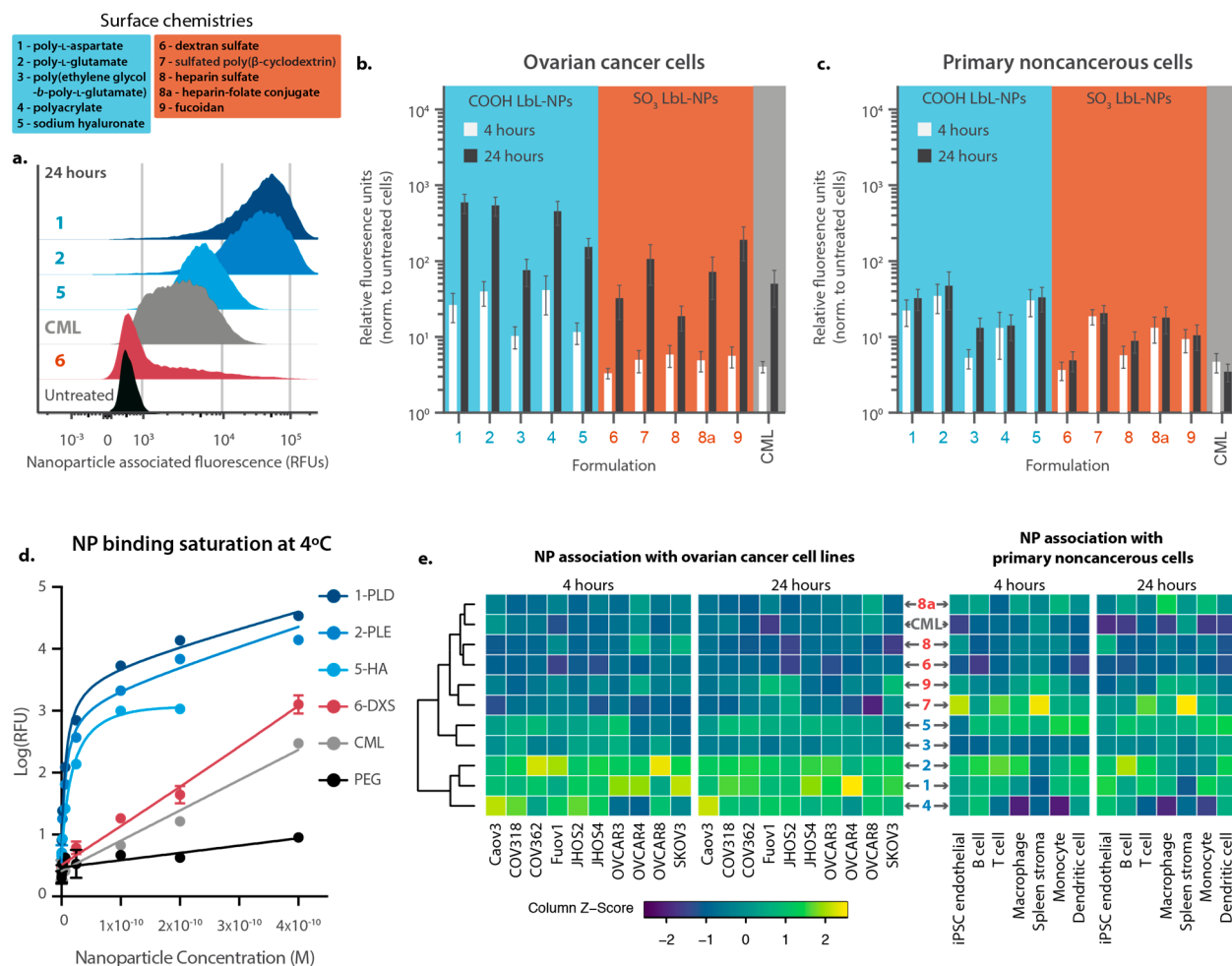


Figure 2. LbL-NPs with carboxylated terminal layers associate preferentially with ovarian cancer cells, in contrast to sulfated LbL-NPs and carboxylated non-LbL NPs. Fluorescent LbL-NPs were incubated with cells from a panel of 10 human ovarian cancer cell lines or seven noncancerous primary cells for 4 or 24 h and then analyzed by flow cytometry to determine nanoparticle-associated fluorescence. (a) Representative flow cytometry results showing nanoparticle association with Caov3 ovarian cancer cells. Pooled median nanoparticle fluorescence intensity for (b) 10 ovarian cancer cell lines and (c) seven primary noncancerous cell types at 4 and 24 h. (d) A binding saturation isotherm was conducted on OVCAR8 cells at 4 °C to calculate apparent K_d values for 1-PLD-NPs, 2-PLD-NPs, 5-HA-NPs, 6-DXS-NPs, and conventional CML-NPs and PEG-NPs. 1-PLD-NPs and 2-PLD-NPs had K_d values of 6.8 ± 1.6 and 6.2 ± 2.2 pM, respectively. 5-HA-NPs had a K_d value of 18.7 ± 18.4 pM. 6-DXS-NPs, PEG-NPs, and CML-NPs could not be fit to the model and appear to act *via* nonspecific binding interactions. (e) Hierarchical clustering of the flow cytometry data from the ovarian cancer cells groups NPs by surface chemistry. Data were column-normalized to facilitate comparison of 4 and 24 h data. In the right panel, results from noncancerous cells are displayed according to the cancer cell clustering. Error bars in (b), (c), and (d) represent SEM.

PLR/CML-NPs are referenced as X-NPs). Overall, these results demonstrate this approach to LbL-NP assembly can generate libraries of NPs that can be used to screen the effects of diverse surface chemistries.

Within the Polymer Library, Carboxylated LbL-NPs Preferentially Bind to Ovarian Cancer Cells Relative to Sulfated LbL-NPs. To determine whether NP surface chemistry governs binding to HGSOc cells, we used flow cytometry to assay NP–cell association in a panel of 10 human ovarian cancer cell lines (Caov3, COV318, COV362, Fuov1, JHOS2, JHOS4, OVCAR3, OVCAR4, OVCAR8, and SKOV3). The median fluorescence intensity ratio (MFIR) between treated and untreated cells was used to quantify NP–cell association at short (4 h) and ultimately longer (24 h) time frames. We found that of the polymers tested, the COOH-LbL-NPs substantially associated with HGSOc cells after sustained time periods, achieving approximately 5-fold enrichment when compared to SO_3 -LbL-NPs after 24 h (Figure 2a,b).

To evaluate how NPs in our panel interact with noncancerous cells, we repeated our NP–cell association experiment using induced pluripotent stem cell (iPSC)-derived endothelial cells and primary immune and stromal cells isolated from murine spleens. We found that our subset of COOH-LbL-NPs was significantly enriched in cancer cells relative to noncancerous cells by 24 h (Figure 2b,c). At 24 h, COOH-LbL-NP binding of HGSOc cells (MFIR of 365.0 ± 62.2) significantly outpaced that of noncancerous cells (MFIR of 28.1 ± 2.1), indicating an average 13-fold specificity for cancer cells (q -value < 0.0001). Individually, PLD (*ca.* 18-fold specificity, q -value < 0.0001), PLE (*ca.* 11-fold specificity, q -value < 0.0001), and polyacrylate (*ca.* 30-fold specificity, PAA, q -value = 0.0004) coated NPs showed significant enrichment in cancer cells by 24 h. In contrast, HA-NPs had a smaller, *ca.* 5-fold specificity despite possessing a ligand-binding capability. This difference may indicate the importance of COOH density, as the HA-NPs are the least densely carboxylated and the PAA-NPs are the most

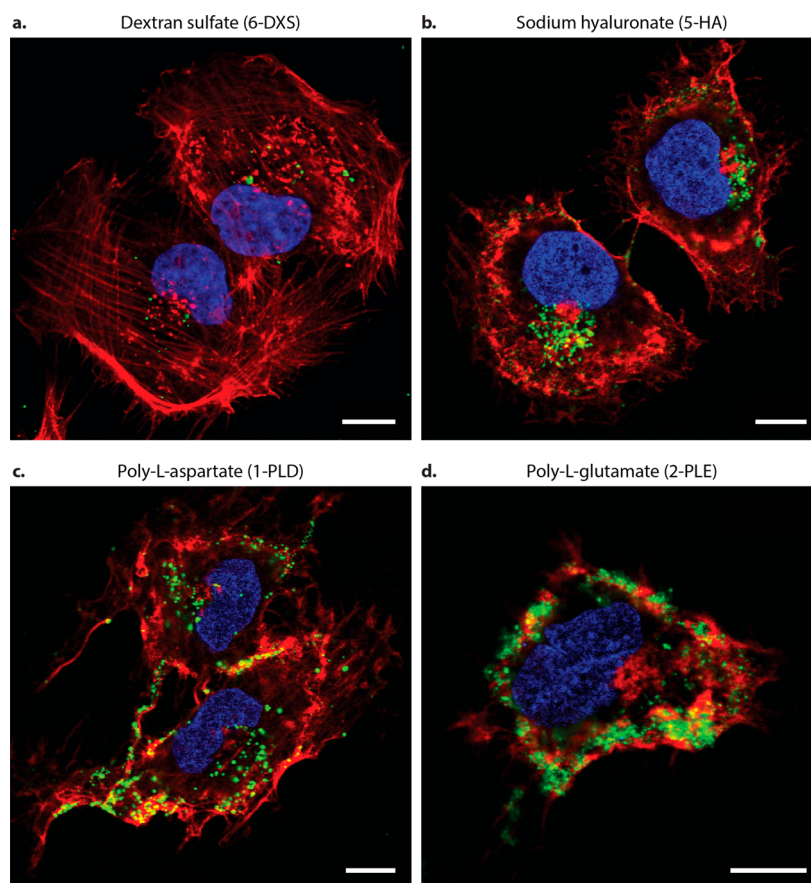


Figure 3. Different carboxylated LbL-NPs possess distinct subcellular fates despite surface chemistry similarities. OVCAR8 cells were incubated with LbL-NPs for 24 h and then fixed and analyzed by confocal microscopy to obtain representative Z-slices. Cell membranes are shown in red, nanoparticles are shown in green, and nuclei are shown in blue. Although less abundant, (a) 6-DXS-NPs bound to OVCAR8 cells were internalized. Relative to 6-DXS-NPs, many more (b) 5-HA-NPs were observed bound and internalized by OVCAR8 cells. (c) 1-PLD-NPs and (d) 2-PLE-NPs also accumulate on OVCAR8 cells, but a significant fraction of NPs remain associated with the membrane for 2-PLE-NPs, whereas the 3-PLD-NPs tended to accumulate at the membrane and then undergo slow caveolae-mediated uptake. Scale bar denotes 10 μm .

carboxylated. In the following experiments, we excluded PAA-NPs in the interest of further characterizing the more biocompatible PLE and PLD surface chemistries. Overall, these COOH-LbL-NPs associated with and were significantly enriched in HGSOC cells when compared to noncancerous cells *in vitro*, indicating that the COOH-rich surface chemistry generated by the LbL adsorbed outer layer shows potential for applications in HGSOC-targeted drug delivery.

SO₃-LbL-NPs Bind Variably to Ovarian Cancer and Can Target Stromal Cells. SO₃-LbL-NPs associated heterogeneously with cells, resulting in poor specificity to HGSOC cells. By 24 h, SO₃-LbL-NPs as a whole accumulated approximately 6-fold more in cancer cells than noncancerous cells (MFIR of 84.4 ± 24.1 and 12.6 ± 2.1 , respectively, q -value = 0.01), though the result was not significant. Individually, none of the SO₃ formulations exhibited preferential association to cancer cells (q -values between 0.2 and 0.7). In general, sulfated LbL formulations had poor tumor-targeting capabilities compared to their carboxylated counterparts. However, the noncancerous cell screen revealed that sulfated poly(β -cyclodextrin) (SBC)-NPs preferentially accumulated in spleen stromal and endothelial cells (Figure 2e, Z -score > 2), indicating a potential utility for SBC-NPs in the delivery of immunotherapy or antiangiogenesis drugs.

PLD- and PLE-Coated Systems Show Higher Affinity than Receptor-Targeted NPs. Active targeting, through the

use of a ligand specific to a cellular surface marker, is the leading approach to improve delivery to specific cell types. Three of our formulations (HA-NPs, HS-NPs, and HF-NPs)^{21–23} possess targeting capabilities without the need for additional coupling chemistries, because the outermost polymers undergo specific binding interactions with their corresponding receptors. Notably, HA-NPs and HF-NPs bind CD44 and folate receptor, respectively, and both are overexpressed on many solid epithelial tumors, including HGSOC. Surprisingly, these NPs showed a clear affinity for HGSOC cells over control NPs, but were not as highly binding as the tested COOH-LbL-NPs (e.g., PLD-NPs, PLE-NPs, PAA-NPs) lacking any known active targeting capability. By 24 h, PLD-NPs and PLE-NPs accumulated roughly 4- and 3.5-fold more HGSOC cells than did HA-NPs. This observation led us to hypothesize that unknown specific binding interactions may be occurring between these polypeptide-coated systems and HGSOC cells.

To investigate whether the binding of PLD-NPs and PLE-NPs could be attributed to specific or nonspecific interactions, we performed a saturation binding study at 4 °C to measure apparent dissociation constants ($K_{d,app}$) for HA-NPs, PLD-NPs, and PLE-NPs (Figure 2d). DXS (dextran sulfate sodium salt)-NPs, CML-NPs, and conventional poly(ethylene glycol)-functionalized NPs (PEG-NPs) were used as controls for sulfated, non-LbL, and antifouling systems, respectively. As anticipated, the binding curve for HA-NPs was characteristic of

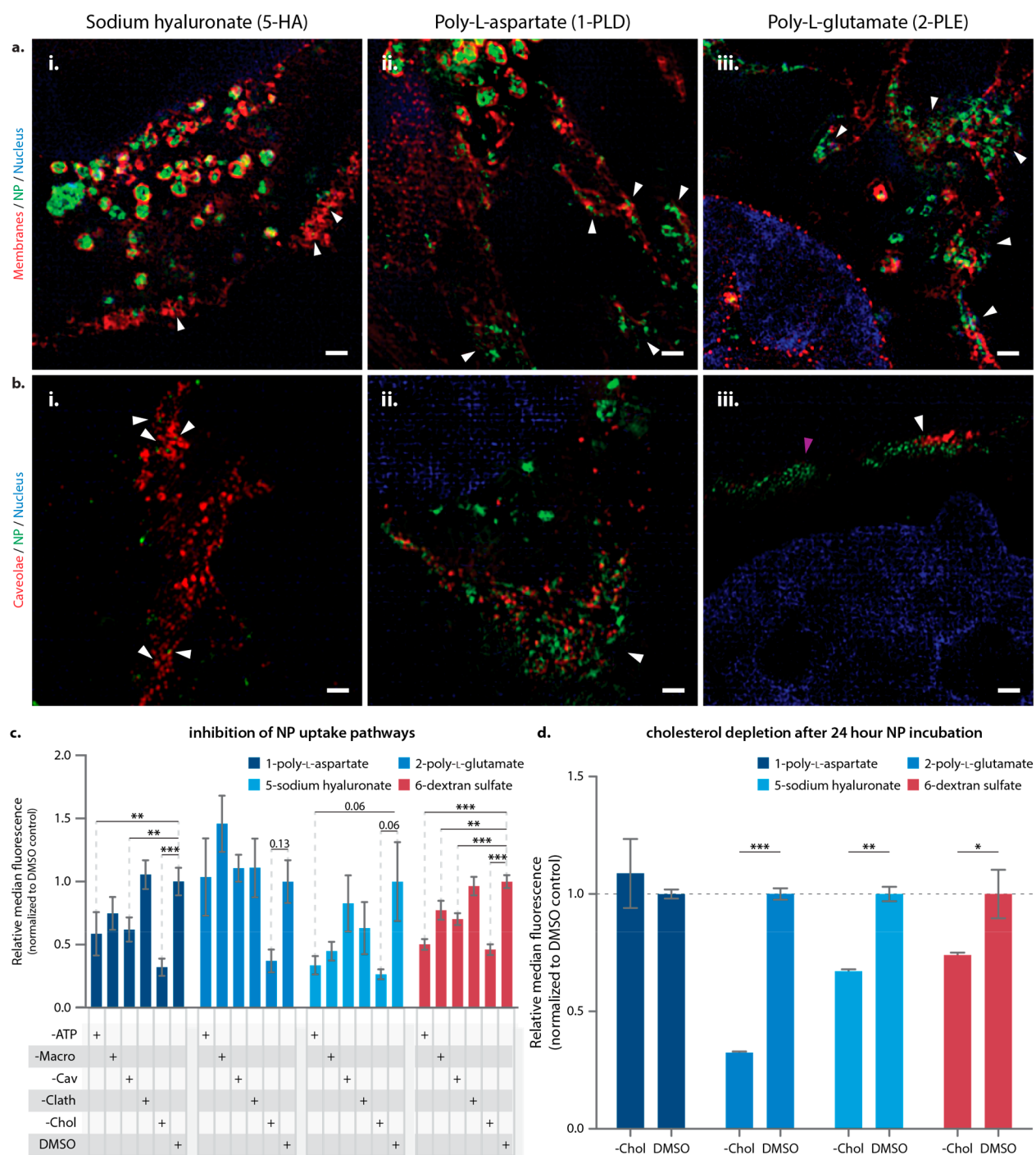


Figure 4. LbL-NP surface chemistry influences uptake pathways in cancer cells. Super-resolution microscopy was used to more precisely determine nanoparticle subcellular fates. (a) High-magnification Z-slices of super-resolution images indicating NP association with wheat-germ agglutinin stained cell membranes. 1-PLD-NPs and 2-PLE-NPs were abundant on the surface membrane. White arrows indicate association with cell membrane. (b) High-magnification Z-slices of NP association with CAV1+ caveolae. 5-HA-NPs were occasionally observed in caveolae. Membrane-bound 1-PLD-NPs were generally associated with caveolae, in contrast to 2-PLE-NPs. White arrows indicate association with caveolae. Purple arrow highlights membrane-bound NPs distant from caveolae. Scale bars in panels (a) and (b) denote 1 μm . (c) OVCAR8 cells were pretreated with endocytosis inhibitors prior to a 4 h incubation with NPs and then analyzed by flow cytometry to determine changes in NP-associated fluorescence. Results are normalized to DMSO controls. (d) To determine if membrane-bound NPs associate to cholesterol-rich lipid rafts, OVCAR8 cells were incubated with NPs for 24 h and then treated with cholesterol-depleting cyclodextrins for 4 h prior to analysis by flow cytometry. Error bars in panels (c) and (d) represent SEM. Multiple comparisons were performed using the FDR approach ($Q = 5\%$) following one-way ANOVA or Student's t test. Asterisks denote discoveries by FDR; *** $q < 0.0002$, ** $q < 0.002$, * $q < 0.047$.

specific interactions, yielding a $K_{d,\text{app}}$ of 18.7 ± 18.4 pM. Notably, the binding curves for PLD-NPs and PLE-NPs also suggested that specific interactions were mediating enhanced

HGSOC targeting. Consistent with our earlier results, PLD-NPs and PLE-NPs had an improved $K_{d,\text{app}}$ of 6.8 ± 1.6 and 6.2 ± 2.2 pM, respectively. In contrast, DXS-NPs, CML-NPs, and PEG-

NPs exhibited classic linear binding curves typical for non-specific interactions. Further study is needed to determine the binding mechanisms between PLE-NPs and PLD-NPs and HGSOC cells, but a potential mechanism may be derived from prior work indicating carboxylated polymers possess mucoadhesive properties,^{24,25} and therefore may bind to mucins overexpressed by HGSOC cells.²⁶

LbL Film Architecture Is Vital for COOH-LbL-NP Affinity to Ovarian Cancer. To determine whether COOH functionalization alone is sufficient to target NPs to HGSOC, we compared COOH-LbL-NPs to uncoated CML-NPs, which are carboxylated but lack the LbL film architecture. We found that CML-NPs had variable cell binding, similar to what was observed for SO₃-LbL-NPs (Figure 2b,c). Overall, CML-NPs associated poorly to HGSOC cells, roughly 7-fold less than COOH-LbL-NPs. Furthermore, hierarchical clustering of the NP-HGSOC binding data set grouped together all COOH-LbL-NPs, while CML-NPs clustered with SO₃-LbL-NPs (Figure 2e). Notably, clustering of the noncancerous cell data set yields clusters with mixed surface chemistries (Figure S2), indicating a surface chemistry preference by HGSOC but not by the noncancerous cells tested here. Overall, these data indicate that the LbL film introduces critical, and tunable, parameters that may reshape the nano–bio interface, which likely include the presence of a hydrated swollen brush-like layer and its physicochemical interactions with cell membranes.

Surface Chemistry Influences Subcellular Targeting.

We hypothesized that if NP surface chemistry governed NP–cell association, it may also govern subcellular trafficking. Determining such structure–activity relationships could therefore inform the design of NPs that preferentially target drugs not only to specific cell types but also to a specific subcellular compartment or intracellular pathway. To that end, we utilized confocal microscopy to image OVCAR8 cells incubated with either PLD-NPs, PLE-NPs, HA-NPs, or DXS-NPs for 24 h. We found that NP surface chemistry influenced subcellular fate, steering NPs to accumulate either at the cell membrane or within endolysosomal compartments. DXS-NPs and HA-NPs were almost exclusively within intracellular compartments at this time point (Figure 3a,b). In contrast, PLD-NPs and PLE-NPs had pronounced localization at the cell membrane (Figure 3c,d). To rule out artifacts from the fixation process and to further validate NP subcellular fate, we analyzed NP trafficking in JHOS4 (Figure S3), COV362 (Figure S4), and Caov3 (Figure S5) lines using live-cell confocal microscopy. These studies confirmed the subcellular trafficking observed in fixed-cell imaging and evaluated the remaining LbL-NPs in the panel, which are discussed in the Supporting Information.

We further studied the subcellular trafficking of PLD-NPs, PLE-NPs, HA-NPs, and DXS-NPs through a systematic super-resolution microscopy (SRM) study in OVCAR8 cells, focusing on association with cell membranes, early endosomes, caveolae, lysosomes, and trans golgi. Consistent with our earlier results, HA-NPs were more internalized, with PLD-NPs and PLE-NPs associated with more of the cell membrane at 24 h (Figures 4a and S6). Co-localization analysis indicated that PLD-NPs and PLE-NPs covered 3× and 25× more of the cell membrane (Figure S7). SRM revealed that PLD-NPs on the cell membrane were slowly taken up over time and generally associated with caveolar vesicles to a greater extent than membrane-bound PLE-NPs (Figures 4b and S8). PLD-NP co-localized with CAV-1 labeled structures 2× more than PLE-NPs and 5× more than HA-NPs (Figure S9). Consistent with our expectations for this

time point, internalized NPs were within late endolysosomal vesicles rather than early endosomes (Figures S10 and S11). PLE-NPs and PLD-NPs appeared to traffic to positions adjacent to trans-golgi membranes (Figure S12), which may suggest NP-containing vesicles are sorted by the trans-golgi network.

To determine if PLD-NPs, PLE-NPs, and HA-NPs use distinct trafficking pathways, we performed an uptake inhibition study to probe the role of ATP-, caveolar-, clathrin-, macropinocytosis-, and cholesterol-mediated uptake (see Table 1 for

Table 1. Inhibitor Molecules Used to Block Nanoparticle Uptake Pathways

targeted pathway	inhibitor
ATP-dependent (-ATP)	sodium azide
macropinocytosis (-Macro)	wortmannin
caveolar (-Cav)	genistein
clathrin-mediated (-Clath)	chlorpromazine
cholesterol-mediated (-Chol)	methyl- β cyclodextrin

the inhibitors used). OVCAR8 cells were pretreated with inhibitors and then incubated with LbL-NPs for 4 h prior to flow cytometry analysis (Figure 4c). We observed that ATP-mediated processes were essential for PLD-NPs and HA-NPs. Inhibition of clathrin, which is involved in receptor-mediated endocytosis, appeared to reduce HA-NP uptake, consistent with a CD44-mediated uptake pathway. However, clathrin inhibition has no effect on PLE and PLD-NPs, suggesting that if these NPs are indeed binding to a specific cell surface feature, it is not subject to clathrin-mediated endocytosis. Consistent with our super-resolution imaging, caveolar inhibition reduced uptake of PLD-NPs but not of PLE-NPs. Cholesterol-mediated uptake was critical for all NPs that exhibited uptake, including DXS-NPs. For PLE-NPs, which tend to remain on the cell membrane, the reduction in NP-associated fluorescence upon cholesterol depletion indicates that cholesterol-associated features on the cell surface are critical for binding PLE-NPs.

To further explore the role of cholesterol, we sought to evaluate if membrane-bound NPs were associated with cholesterol-rich lipid rafts. OVCAR8 cells were incubated with LbL-NPs for 24 h and then treated with methyl-beta cyclodextrin to deplete cholesterol prior to flow cytometry (Figure 4d). This treatment extracts cholesterol directly from the cell membrane, disrupting lipid rafts and lipid-associated macromolecules, which we hypothesized would free NPs associated with these structures. Notably, the PLE-NP-treated cells had 68% lower NP signal after cholesterol depletion (q -value = 2×10^{-5}), whereas PLD-NP-treated cells were unaffected (9% increase, q -value = 0.3). HA-NP-treated cells saw a small but significant impact (33% decrease, q -value = 5×10^{-4}), which we attributed to cholesterol's involvement in facilitating membrane budding during endocytic uptake. Overall, these data suggest an early role for cholesterol in the binding of PLE and PLD-NPs, where the NPs associate with cholesterol-rich regions of the cell membrane, regions that in ovarian and breast cancer cells are enriched with mucins.^{27–29} But at later time points, PLD-NPs cease to be associated with cholesterol, as they are internalized *via* caveolae. In contrast, PLE-NPs are highly dependent on cholesterol throughout the studied time points, suggesting PLE-NPs remain associated with cholesterol-associated features over time. These differences between PLE and PLD formulations are striking, as these polymers differ by a single methylene group.

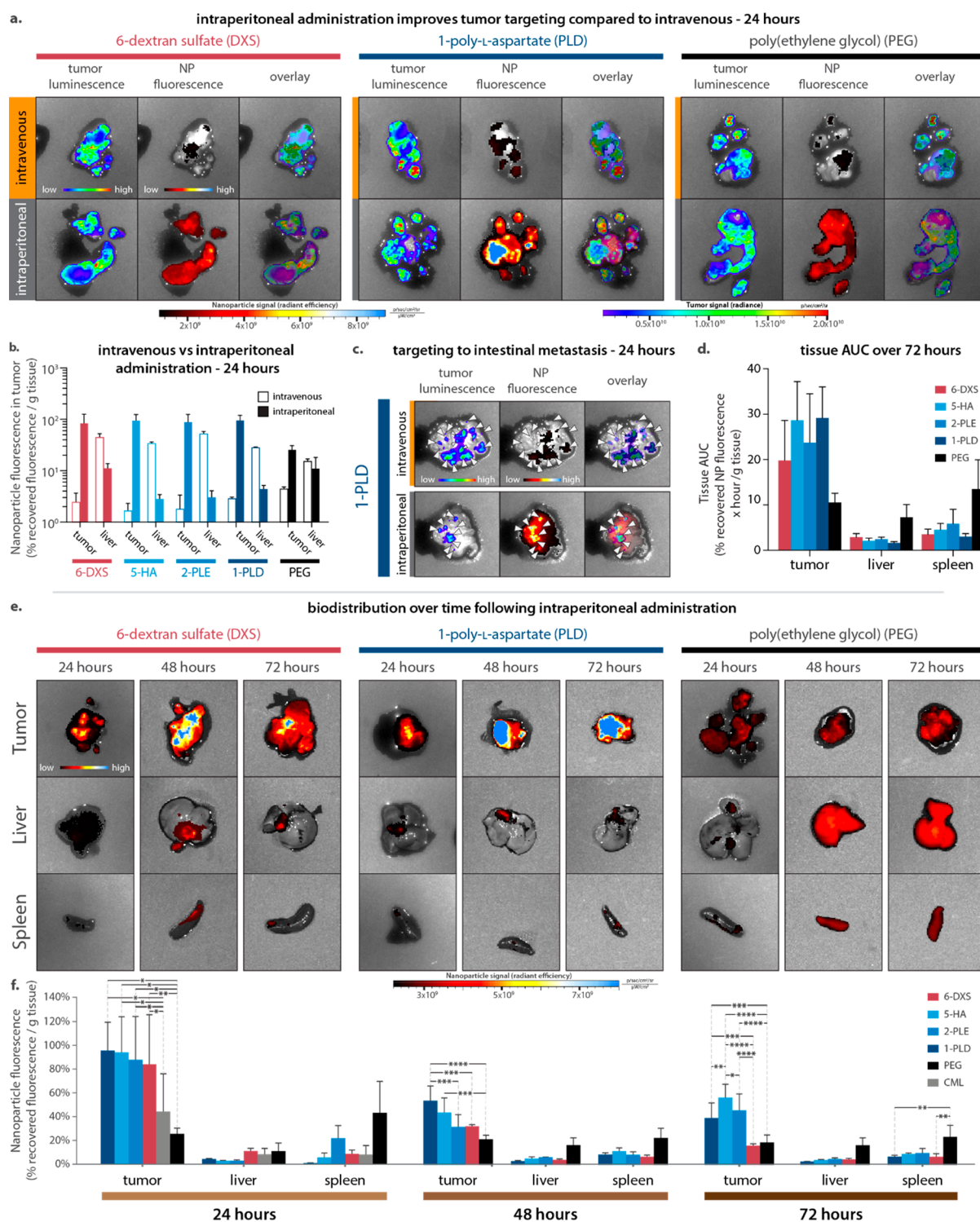


Figure 5. Tracking NP biodistribution in an orthotopic model of ovarian cancer reveals a durable accumulation of COOH LbL-NPs in neoplastic tissue relative to 6-DXS-NPs and PEG-NPs. NPs were administered IP or IV to murine models of metastatic ovarian cancer, and infrared fluorescence from nanoparticles was measured for each organ at the indicated time points. (a) Comparison of tumor accumulation following IP or IV administration of nanoparticles. (b) Quantification of the mean percent recovered NP fluorescence per gram of tumor following IP or IV administration. (c) Representative images of PLD-NPs accumulating in intestinal metastases by 24 h after either IP or IV administration. Refer to (a) for scale bars. (d) Tissue AUC for tumor, liver, and spleen over 72 h for each NP formulation following IP administration. (e) Representative images of NP biodistribution over 72 h following IP administration. (f) Quantification of percent recovered NP fluorescence per gram of tissue at 24, 48, and 72 h indicated that COOH LbL-NPs had significant and improved accumulation in neoplastic tissue relative to 6-DXS-NPs, PEG-NPs, or CML-NPs. Data were compiled from three independent experiments. CML-NPs were tested only at 24 h. Error bars represent SEM, $n = 3, 4$ for (b) and (f). Multiple comparisons were performed using the FDR approach ($Q = 5\%$) following 2-way ANOVA. Asterisks denote discoveries by FDR; $****q < 0.0001$, $***q < 0.001$, $**q < 0.01$, $*q < 0.045$.

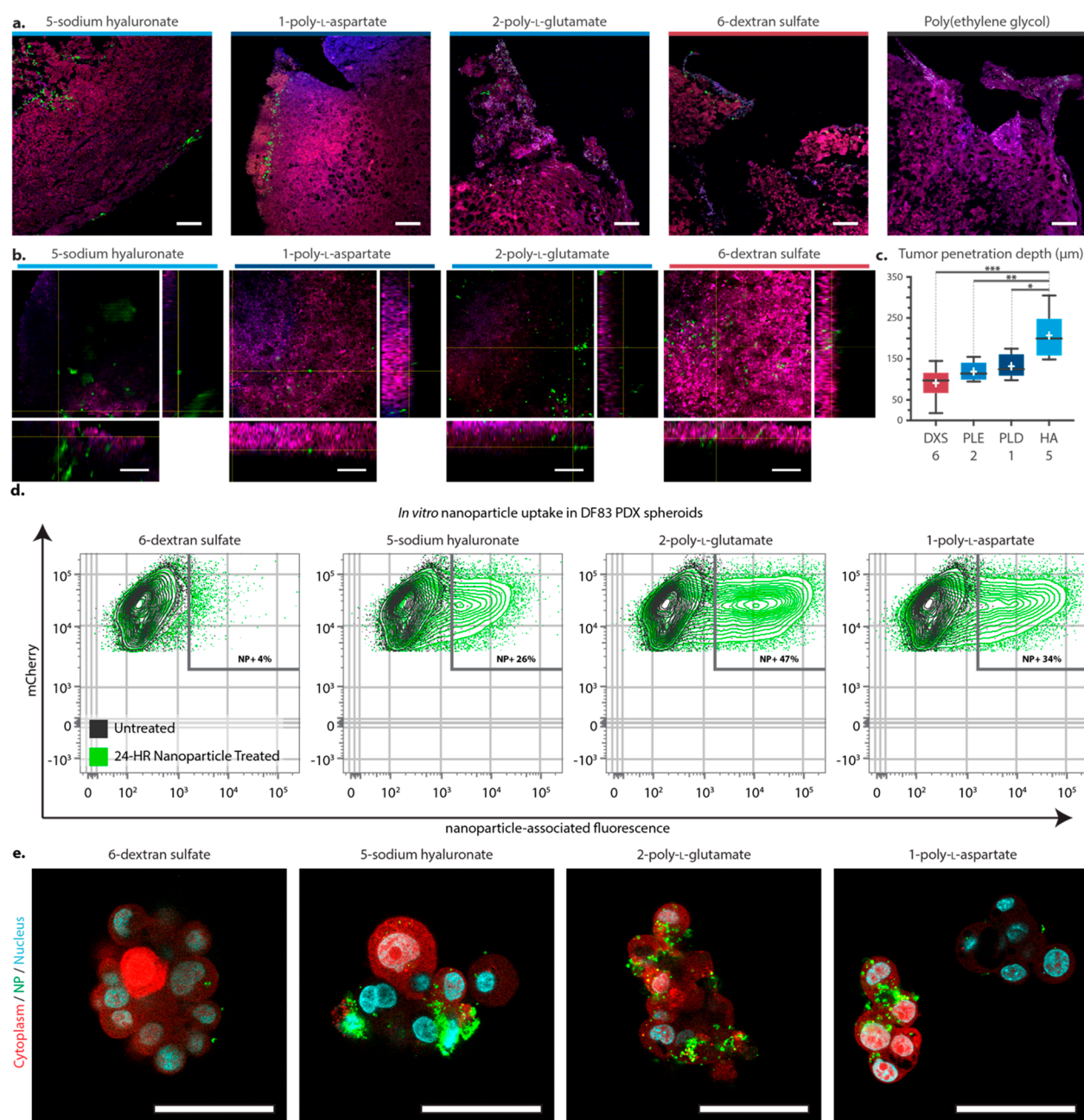


Figure 6. LbL-NPs penetrate into tumor tissue and patient-derived xenograft spheroids. NPs were administered IP to mice bearing orthotopic ovarian cancer xenografts, and after 24 h, tumors were collected and processed for histology or multiphoton whole-tissue imaging. (a) Fluorescence imaging of tumor sections 24 h after NP administration revealed NPs accumulate on the tumor surface, with some penetration into the tissue. Red and blue signals are pseudocolored autofluorescence from H&E staining; green signal indicates nanoparticle. (b) Representative slices and orthogonal views of z -stacks acquired from whole-tumor imaging using multiphoton microscopy. Blue signal corresponds to collagen autofluorescence, red corresponds to the mCherry signal from tumor cells, and green signal is from nanoparticles. (c) Z -stacks were quantified to measure NP penetration into tumor tissues. HA-coated NPs penetrated the deepest into tissue with an average depth of $200.0 \pm 23.4 \mu\text{m}$. Whiskers indicate minimum and maximum values, $n = 6$ for quantification of multiphoton imaging. (d) mCherry-expressing PDX spheroids were cultured with NPs *in vitro* for 24 h and then processed for flow cytometry. Single live cells were analyzed for association with NPs. (e) PDX spheroids were incubated with NPs for 24 h and then fixed and analyzed using confocal microscopy to obtain representative z -slices. Scale bars denote $100 \mu\text{m}$ in panels (a) and (b) and $50 \mu\text{m}$ in (e). Multiple comparisons were performed using the FDR approach ($Q = 5\%$) following one-way ANOVA. Asterisks denote discoveries by FDR; *** $q = 0.0002$, ** $q = 0.0018$, * $q = 0.0043$.

COOH-LbL NPs Have Superior Tumor Targeting *in Vivo*. To determine if COOH-LbL-NP targeting of HGSOc *in vitro* translated to enhanced NP tumor delivery *in vivo*, we performed biodistribution studies in an orthotopic model of HGSOc with PLD-NPs, PLE-NPs, HA-NPs, DXS-NPs, CML-NPs, and PEG-NPs. We evaluated NP biodistribution using

both systemic (IV) and intraperitoneal (IP) administration methods. We assessed IP administration because metastatic HGSOc is compartmentalized to the organs of the IP space,^{17,18} and clinical trials have found benefits to IP delivery of chemotherapy.^{30–32} However, NPs quickly clear from the IP space,³³ unless they are able to bind to available surfaces.³⁴ We

hypothesized that the COOH-LbL-NPs could tether themselves to the exposed surfaces of tumors and thereby prevent premature lymphatic clearance.

IP administration substantially improved tumor delivery for all NPs (Figures 5a, S13–S19), likely attributable to fewer biological barriers standing between direct NP–tumor interactions when compared to IV administration. More specifically, IV administration yielded 1–5% of recovered nanoparticle fluorescence per gram of tumor, while IP administration of the same NPs increased this metric of tumor accumulation 5- to 60-fold, depending on the surface chemistry (Figure 5b). The only LbL-NP-enriched regions in peripheral organs were metastatic lesions (Figures 5c, S20–24). Impressively, 24 h after IP administration, the bulk of recovered LbL-NP signal was associated with tumor tissues, persisting out to 72 h (Figure 5c–f). During this time, COOH-LbL-NPs avoided clearance to the liver or spleen. Consistent with our prior results, COOH-LbL-NPs accumulated significantly more in tumor tissue than DXS-NPs, CML-NPs, or PEG-NPs.

While CML and PEG-NPs also benefited from IP administration, PEG-NPs began accumulating in the liver and spleen by 24 h, leading to approximately 4- and 3-fold higher PEG-NP signal in these tissues by 72 h, relative to LbL-NPs. We attribute this to the antifouling properties of PEG promoting rapid lymphatic drainage from the IP space. Taken together, these results indicate that COOH-LbL-NPs selectively accumulate in ovarian tumors after IP administration and avoid lymphatic clearance, providing a platform to more selectively deliver antitumor drugs to ovarian cancer.

Active Targeting Ligands May Enhance Tissue Penetration. To examine NP distribution within the tumor, we performed histology on tumors 24 h after NP treatment (Figure 6a). We found that NPs accumulated on the surfaces of tumor tissues, consistent with our hypothesis that IP-administered NPs bind to the tumor surface to avoid rapid lymphatic drainage. Interestingly, HA-NPs penetrated deeper into tissue than did other NPs. To further investigate NP penetration depth, we performed whole-tissue multiphoton microscopy on tumors from mice 72 h after NP treatment. We found that the average NP penetration depth ranged from 100 to 200 μm , with HA-NPs penetrating deepest into the tissue (Figure 6b). Quantification of these images indicated that PLD ($132.2 \pm 12.1 \mu\text{m}$) and PLE ($119.3 \pm 9.6 \mu\text{m}$) NPs tended to penetrate deeper than DXS (91.3 ± 17.2) NPs, which is consistent with our prior *in vitro* and *in vivo* studies. HA-NPs entered significantly deeper into tumors than the other NPs (*q*-values between 0.004 and 0.0001), with an average penetration depth of 207.5 ± 23.4 (Figure 6c). While past research has found that high-affinity interactions inhibit NP penetration into tumors, HA LbL films exhibit antifouling and swelling behaviors that may introduce competing forces that drive deeper penetration into tumors.²¹ Notably, PEG-NPs were not detectable using consistent acquisition conditions and could not be quantified. The results from whole-tissue imaging indicate LbL-NPs navigate into tumor tissue after IP administration. They also suggest the ligand-binding capabilities of HA-NPs may facilitate deeper tissue penetration depths, particularly important for IP cancers with dense desmoplastic stroma, such as pancreatic adenocarcinoma.

Enhanced Affinity with COOH-LbL NPs Validated in a PDX Spheroid Model. In patients, free-floating cancer spheroids make up a difficult-to-reach subpopulation with tumor-regenerating, stem-like properties.¹⁷ To determine if

COOH-LbL-NPs could target tumor spheroids, we screened HA-NPs, PLD-NPs, PLE-NPs, and DXS-NPs on HGSOc patient-derived xenograft spheroids. We performed flow cytometry to quantify NP–cell binding following 24 h of incubation with NPs (Figure 6d). Consistent with our prior results, PLD and PLE-NPs bound the most to PDX spheroids (34% and 47% NP+ cells, respectively), followed by HA-NPs (26% NP+). As anticipated, DXS-NPs had minimal binding to the PDX spheroids (4% NP+). We then characterized the spatial localization of the NPs using scanning confocal microscopy on fixed PDX spheroids (Figure 6e). PLD and PLE-NPs were located on the membranes of outermost cells of the spheroids, while HA-NPs were observed mostly intracellularly. Altogether, these data provide further evidence that COOH-LbL-NPs examined here possess a strong affinity for HGSOc cells, whereas SO₃-LbL-NPs do not. Abundant binding of COOH-LbL-NPs to PDX spheroids suggests that NPs functionalized with these coatings have clinically relevant delivery capabilities.

CONCLUSIONS

We performed an unbiased screen of nanoparticle surface chemistry using the LbL platform to map out structure–activity relationships for diverse chemistries including polypeptides, native polysaccharides, and synthetic polymers. Notably, this study identified LbL-NPs with carboxylated surface chemistries possess a striking affinity to ovarian cancer cells, a specificity that was not recapitulated with architecturally similar anionic or non-LbL NPs. These results indicate that LbL films may provide unexpected interactions between nanoparticles and particular cell types that can help to steer NPs to specific tumor cell types and to extra- or intracellular regions of the tumor cell. Interestingly, while carboxylated LbL-NPs shared a high affinity toward HGSOc, subcellular trafficking of the individual surface chemistries preferentially targeted either the cell membrane or perinuclear vesicles, providing insight into subcellular targeting critical for applications such as photodynamic therapy and gene delivery. The tumor-homing abilities of carboxylated LbL-NPs were further validated with PDX spheroids *in vitro* and in an orthotopic model of ovarian cancer, where poly-L-aspartate, poly-L-glutamate, and hyaluronate-coated NPs avoided clearance and demonstrated a highly specific association with neoplastic tissues. These nanoparticles achieved superior tumor-targeting than conventional, PEGylated nanoparticles, the current standard for clinically approved nanomedicines. Excitingly, these findings, combined with the diversity and modularity of LbL films, suggest that there are significant opportunities for future work to identify biomedically relevant surface chemistries. Mapping out this landscape will help to unlock a deeper understanding of structure–activity relationships, allowing researchers to better design NPs suited for particular diagnostic or therapeutic applications.

METHODS

Materials and Reagents. The polyelectrolytes dextran sulfate sodium salt (DXS, 6.5–10 kDa; Sigma-Aldrich), poly(acrylic acid) (PAA, 15 kDa; Sigma-Aldrich), poly(L-arginine) (PLR, 9.6 kDa; Alamanda Polymers), poly(L-glutamic acid) (PLE, 15 kDa; Alamanda Polymers), poly(L-aspartic acid) (PLD, 14 kDa; Alamanda Polymers), poly(ethylene glycol-*b*-poly-L-glutamic acid) (PEG-PLD) (30 kDa PLD, 5 kDa PEG; Alamanda Polymers), hyaluronic acid (HA, 20 kDa; LifeCore Biomedical), sulfated beta-cyclodextrin polymer (18 kDa; Cyclodextrin Technologies), and fucoidan (57 kDa; Santa Cruz Biotechnology) were used without modifications. Heparin sodium salt (HS, unfractionated; Celsus Laboratories) was used both

unmodified and as a conjugate with folic acid (Sigma-Aldrich) as described previously.¹⁶

The fluorescent, carboxylate-modified latex nanoparticles (100 nm, blue fluorescent (350/440), 100 nm yellow-green fluorescent (505/515), 100 nm infrared (715/760); Life Technologies) were used without modification for LbL-NP assembly. For PEGylated control NPs, the latex particles were modified with 3 kDa PEG (JenKem USA) according to the manufacturer's instructions.

Cell Lines. Caov3, OVCAR3, and SKOV3 cell lines were purchased from ATCC (catalog numbers HTB-75, DSMZ ACC 444, HTB-161, and HTB-77). Fuov1 cells were purchased from DSMZ (catalog number ACC 444). COV362, COV318, JHOS2, and JHOS4 cell lines were donated to us by the Drapkin lab. OVCAR4 and OVCAR8 cell lines were donated by the Bhatia lab. All cancer cell lines were authenticated using STR profiling. All cell lines were tested for mycoplasma contamination periodically, including immediately upon thawing and over time when in culture, using the Lonza MycoAlert kit (Catalog #: LT07-318). Results were always negative for mycoplasma contamination.

OVCAR8 cells were engineered to express mCherry and luciferase as described previously.³⁵ Briefly, the dual mCherry/luciferase reporter was constructed using lentiviral pFUW backbone (Addgene). Firefly luciferase-E2A-mCherry was amplified and connected by overlapping PCR and cut by the restriction enzymes *Bam*HI and *Eco*RI. E2A is a self-cleaving peptide sequence, so immediately after translation the fusion protein is split into separate luciferase and mCherry in mammalian cells.

Synthesis of Layer-by-Layer Nanoparticles. LbL nanoparticles were prepared as described previously.¹⁶ Briefly, carboxylate-modified latex nanoparticles (Thermo Fisher) were coated with poly(L-arginine) in Milli-Q water, with no added salts. The deposition step was carried out by adding an equal volume of 1 mg/mL CML core to 4 mg/mL PLR while under sonication (Branson bath sonicator). The mixture was allowed to sonicate for 5 s, then left to incubate at room temperature (RT) for 1 h. The nanoparticles were then purified using tangential flow filtration (Spectrum Laboratories, KrosFlo II system) with a 100 kDa molecular weight cutoff filter (Spectrum Laboratories, D02-E100-05-N). The filter was pretreated with a 4 mg/mL solution (10 min, continuous flow with permeate valve closed) of PLR. The nanoparticle was washed until five volume equivalents were collected in the permeate, using Milli-Q water as the exchange buffer. The CML/PLR particles were then split into different batches to be coated with the various polyanions, using the same steps outlined above for PLR but using a different filter cassette. The filter cassette for anionic layers was not pretreated with polymer solution. The core-to-polymer mass ratios for each polyanion were determined from polyelectrolyte titrations that identified optimal ratios that provided complete charge conversion, which was between 40 and 60 mV for PLR and -40 to -60 mV for the anionic layer. NPs were synthesized under salt-free conditions, which increases variability during layering,¹⁵ and thus titrations should be performed to identify the optimal ratio for each new synthesis. The starting ratios used for each polyelectrolyte were 1:6 for heparin sulfate folate conjugate; 1:10 for heparin sulfate and fucoidan; 1:8 for dextran sulfate; 1:24 for randomly sulfated beta cyclodextrin; 1:6 for poly(ethylene glycol-*b*-poly-L-glutamate); 1:4 for hyaluronic acid, poly(L-aspartate), and poly(L-glutamate); and 1:3 for polyacrylate. No salts were added during the deposition or purification steps for the polyanion layers.

Nanoparticle Characterization. Nanoparticle hydrodynamic size and polydispersity were measured using dynamic light scattering (Malvern ZS90 particle analyzer, $\lambda = 633$ nm, material/dispersant RI 1.590/1.330). Zeta potential measurements were also acquired with the Malvern ZS90, using laser Doppler electrophoresis. Nanoparticle solutions were diluted in Milli-Q water, with no added salts, in polystyrene semimicro cuvettes (VWR) or DTS1070 folded capillary cuvettes (Malvern) to produce samples for characterization. TEM was performed with a JEOL 2011 high contrast digital TEM (120 kV). Nanoparticle solutions were drop casted onto mesh copper grids coated with continuous carbon films to produce specimens for TEM.

Binding Assay for Ovarian Cancer and Noncancerous Cells. The ovarian cancer cell lines and iPSC-derived endothelial cells were

seeded onto 96-well plates (Nunc) at a density of 15 000 cells per well in 100 μ L of the serum-supplemented media corresponding to each cell line. Caov3, COV318, and COV362 were grown in DMEM media (Corning) supplemented with 10% fetal bovine serum (FBS) and 2 mM L-glutamine (Gibco). Fuov1, JHOS2, and JHOS4 cells were grown in DMEM:Ham's F-12 (1:1) (Corning) supplemented with 10% FBS. Media for the JHOS lines was further supplemented with 0.1 mM MEM nonessential amino acids (Gibco). OVCAR3, OVCAR4, and OVCAR8 lines were grown in RPMI-1640 media (Corning) supplemented with 10% FBS. OVCAR3 cells were further supplemented with 0.01 mg/mL bovine insulin (MilliporeSigma). SKOV3 cells were grown in McCoy's 5A media (Corning) supplemented with 10% FBS. Induced-pluripotent stem cell-derived endothelial cells (iPSC-ECs; Cellular Dynamics International) were grown in Lifeline, Vasculife VEGF medium kit, substituting FBS with media supplement obtained from CDI, according to the manufacturer's instructions. Splenocytes were harvested from homogenized whole mouse (Balb/C female) spleens and seeded at a 500 000 cell per well density. Splenocytes were grown in RPMI-1060 media supplemented with 10% FBS, 0.1 mM MEM nonessential amino acids, 1% sodium pyruvate, and 50 μ M 2-mercaptoethanol. All media was supplemented with 1% penicillin-streptomycin. All cells were allowed to adhere/grow for 24 h before treatment with nanoparticles in a Heracell Incubator (Thermo Fisher) at 37 °C and 5% CO₂.

Green fluorescent nanoparticle compound plates were prepared in polystyrene v-bottom 96-well plates (Corning) and standardized to a concentration of 130 μ g polystyrene/mL Milli-Q water. A TECAN Freedom Evo 150 with an MCA96 head was used to mix the nanoparticles in the compound plate, transfer 5 μ L of the nanoparticle solution, and gently mix it in the cell assay plate. Cells were allowed to incubate with nanoparticles for 4 and 24 h, and then the plates were washed three times with phosphate-buffered saline (PBS), and 20 μ L of trypsin-EDTA was added to the cells using a BioTek EL406 plate washer. The cells were incubated for 5 min at 37 °C to dissociate them from the tissue culture plastic. The TECAN Freedom Evo 150 was then used to add 80 μ L of DMEM supplemented with 10% FBS to each well and to mix the cells into a single-cell suspension. Resuspended cells were then analyzed using an iQue high-throughput flow cytometer, and nanoparticle fluorescence data were collected in the FL1-A channel.

For splenocytes, the protocol differed in order to identify specific cell populations. Splenocyte plates were spun down at 500 RCF for 5 min to pellet suspension cells. The supernatant was removed using the BioTek EL406 plate washer, and 20 μ L of trypsin EDTA was added to each well to dissociate any adherent cells from the plate surface. An 80 μ L amount of complete DMEM was added as described above, and then the cells were spun again at 500 RCF for 5 min and washed with PBS. Dead cells were labeled using live/dead aqua stain (BioLegend), according to the manufacturer's protocols. Cells were pelleted again as described above and then resuspended in 80 μ L of PBS supplemented with 3% bovine serum albumin (BSA). A 2 \times antibody master with Fc block (BioLegend, 101302) mix was prepared to label specific cell types and then added to each well using a multichannel repeater pipet (Integra). The cells were incubated in the antibody mix for 30 min at 4 °C and then washed twice with 3% BSA PBS prior to analysis on a BD Fortessa cytometer. The antibodies used were APC CD45 (hematopoietic marker, BD, clone 30-F11), APC-Cy7 B220 (B cell marker, eBioscience, clone RA3-6B21), PE CD3 (T cell marker, BioLegend, clone 17A2), PE-Cy7 CD11b (leukocyte marker, BioLegend, clone M1/70), PerCP-Cy5.5 F4/80 (macrophage marker, Biolegend, clone BM8), and BV605 CD11c (dendritic cell marker, Biolegend, clone N418).

All data were analyzed using FlowJo software. Single-color flow was analyzed without compensation. The splenocytes were analyzed using the appropriate compensation matrix generated from single-color controls. Populations were gated such that only single cells (and live cells in the case of the splenocytes) were quantified for nanoparticle-associated fluorescence. The median nanoparticle-associated fluorescence was determined for each population and imported into an R workspace for further analysis. Triplicates for each treatment condition for each cell type were averaged and then normalized to the average

median fluorescence value acquired for corresponding cells that were not treated with nanoparticles to generate a median fluorescence intensity ratio (MFR). The MFR of the different ovarian cancer cells were combined to visualize uptake in Figure 2, as were the data for noncancerous cells. The data for both time points were used to generate a clustered heatmap using the heatmap.2 function in the gplot package in R. Clusters were calculated using the built-in Euclidean distance function.

NP Binding Isotherm. OVCAR8 cells were trypsinized and washed in complete RPMI media to generate a cell suspension at 500 000 cells/mL in 4C media. A total of 50 000 cells were added to each well (100 μ L) of a v-bottom 96-well plate. Serial dilutions of nanoparticles were prepared in a deep v-bottom 96-well compound plate. Both plates were chilled to 4 °C. A TECAN Freedom Evo 150 was used to premix the nanoparticle compound plate, transfer 100 μ L of 2 \times nanoparticle solution, and mix into each well of the OVCAR8 suspension plate, which was then kept on ice for 1 h. Afterward, the treatment plate was spun at 500 RCF and the supernatant was removed using a BioTek EL406 plate washer. Cells were washed with 200 μ L of PBS and recentrifuged. The cells were then resuspended in live/dead far-red stain (BioLegend) at 4 °C for 15 min. The cells were recentrifuged and then resuspended in 100 μ L of 1 μ g/mL Hoechst in PBS for 5 min. Finally the cells were recentrifuged one last time and resuspended in 80 μ L of ice cold PBS. The plates were then analyzed using a BD LSR2 cytometer. All data were analyzed on FlowJo, and the populations were gated such that only single cells that were Hoechst+ and red- cells were analyzed. The Hoechst stain eliminated the chance that any nanoparticle aggregates from the highest concentration conditions might be mistaken for cells on the cytometer. Median fluorescence intensity data were exported to Prism GraphPad software, where they were fit using the one site-total binding model without any constraints.

Live Cell Confocal Imaging. COV362 and Caov3 cells were seeded on 35 mm MatTek glass bottom dishes and allowed to adhere for 24 h. JHOS4 cells were seeded onto black glass-bottom 96-well plates and also allowed to adhere for 24 h. Cells were treated with 20 pM concentrations of blue-fluorescent nanoparticles and analyzed after a 24 h incubation. Prior to imaging, cells were stained for using AlexaFluor 555 wheat germ agglutinin at 10 μ g/mL in serum-free imaging media to label the cell membrane. LysoTracker red was also added and used to label lysosomes following the manufacturer's protocol. Nuclei were labeled using the NucRed dye, also according to the manufacturer's protocols. The cells were imaged using a 20 \times or 60 \times objective on a Nikon A1R confocal microscope using the 405, 488, 561, and 640 laser lines. The filter cubes used were 450/50, 525/50, and 595/50. Images were linearly adjusted to improve contrast and then pseudocolored.

Fixed Cell Confocal Imaging of Nanoparticle Subcellular Trafficking. LabTek chambered glass slides were coated with rat tail collagen (300 μ L of 50 μ g/mL in 0.02 N acetic acid). After 1 h, the wells were washed with PBS and OVCAR8 cells were seeded at 15 000 cells per well. The cells were allowed to adhere for 24 h prior to treatment with a 20 pM concentration of green fluorescent LbL nanoparticles. Cells were incubated for 4 or 24 h, depending on the desired time point, at which time the cells were washed three times with PBS and fixed in 4% methanol-free formaldehyde prepared in PBS (15 min, room temperature). The cells were then washed in ice cold PBS three times (5 min per wash). For all intracellular stains except for CAV1, cells were treated with blocking buffer (0.025% saponin and 5% goat serum in 1 \times PBS) for 1 h. Blocking buffer was removed and replaced with a primary antibody diluted in antibody diluent buffer (0.025% saponin and 1% BSA in 1 \times PBS). The antibody dilutions used were as follows: EEA1 (CST) 1:200; RAB5 (CST) 1:100; RAB7 (CST) 1:400; LAMP1 (Abcam) 1:400; and RCAS1 (CST) 1:400. Cells were incubated in the primary antibody stain overnight at 4 °C, then washed three times in PBS (5 min per wash). The anti-rabbit AF647 Fab fragment (CST) was diluted 1:1000 in antibody diluent buffer and added to the cells. After 1 h at room temperature, the cells were once again washed three times with PBS (5 min per wash) and then stained with DyLight 554 phalloidin, according to the manufacturer's protocols. Afterward, the phalloidin solution was discarded and replaced with a 1 μ g/mL Hoechst

PBS solution (2 min incubation). Finally, the cells were washed three more times in PBS (5 min per wash), and the chamber walls were removed following the manufacturer's instructions. A #1.5 glass coverslip was then mounted using ProLong Antifade Diamond. Nail polish was used to seal the coverslip, and the slide was allowed to cure for 24 h prior to imaging. For CAV1 staining, a Triton-X-based permeabilization technique was used instead. The permeabilization step occurs after fixation and uses a 0.2% Triton-X100 in 1 \times PBS solution. Afterward, blocking is performed using a 1 \times PBS solution supplemented with 10% goat serum and 0.1% Tween 20 (30 min, room temperature). The antibody diluent buffer used in the Triton-X protocol was 1% BSA and 0.1% Tween 20 in PBS. The CAV1 antibody was used at a 1:1600 dilution.

Specimens were imaged using an FV1200 Olympus laser scanning confocal microscope using a 60 \times silicon oil objective, 1.30 NA, and the 405, 473, 559, and 635 laser lines. Hoechst and nanoparticle signals were captured using the standard PMT detectors with filter cubes of 430–455 nm and 490–540 nm, respectively. The phalloidin and organelle signals were collected using the high-sensitivity detectors with filter cubes of 575–620 nm and 575–675 nm, respectively. Image LUTs were linearly adjusted to improve contrast on FIJI and were pseudocolored.

3D-Super-resolution Microscopy of Nanoparticle Subcellular Trafficking. The protocol used above for fixed cell imaging was modified to suit the requirements of the Applied Precision DeltaVision-OMX super-resolution microscope. Namely, instead of LabTek chambered glass slides, chambered coverglass was used. Instead of treating with 20 pM NPs, cells were treated with 4 pM NPs to maintain NP signal within the instrument's dynamic range. Also, after fixation, cells were washed three times with Hank's buffered saline solution (5 min per wash) and stained with AlexaFluor 647 wheat germ agglutinin (WGA, 10 μ g/mL in Hank's buffered saline solution, 10 min). The cells were washed three times with PBS (5 min per wash) and then refixed using 4% formaldehyde for 2 min at room temperature. The phalloidin staining step was omitted on the super-resolution samples, and the Hoechst stain was increased to a 1.25 μ g/mL stain. After staining, the cells were refixed using 1% formaldehyde solution for 5 min at room temperature. Following three more rounds of washing with PBS, the wells were filled with 5 drops of VectaShield (H-1000) and stored in the dark at 4 °C until imaged. The cells shown in Figure 3b,c and Figure S6 were only stained with WGA and Hoechst and were not processed further with any permeabilization agents.

The cells were imaged with a Delta OMX-V4 Blaze 3D structured illumination microscope (Applied Precision, now GE), equipped with 405, 488, 563, and 647 nm lasers and three sCMOS cameras. Images were acquired with a 60 \times , NA 1.43 oil objective, at 0.125 μ m z steps, using 1.518 immersion oil at RT. All images were acquired under the same illumination settings and then processed with OMX softWoRx software (Applied Precision/GE). Images were saved as tiff. Image LUTs were linearly adjusted to improve contrast on FIJI and were pseudocolored.

Uptake Inhibitor Study. OVCAR8 cells were seeded at 20 000 cell/well in 96-well plates 24 h prior to any further treatment. Drug compound plates were prepared in deep-well v-bottom 96-well plates containing complete media containing inhibitors for specific uptake processes. Sodium azide (0.65 mg/mL) and 2-deoxy-D-glucose (8.2 mg/mL) were used to inhibit ATP-mediated processes. Wortmannin (4.3 μ g/mL) was used to inhibit macropinocytosis. Genistein (54 μ g/mL) was used to inhibit caveolar uptake. Chlorpromazine (3.6 μ g/mL) was used to inhibit clathrin-mediated uptake. Methyl-beta cyclodextrin (6.6 mg/mL) was used to deplete cholesterol and thereby inhibit cholesterol-mediated uptake. Wortmannin, genistein, and chlorpromazine were prepared using 200 \times DMSO master stocks. An equivalent amount of DMSO was added to the water-soluble inhibitor solutions to eliminate DMSO as a variable. DMSO-only controls were used as well. Nanoparticle master plates were prepared in v-bottom 96-well plates at 130 μ g polystyrene/mL Milli-Q water.

Cell assay plates were washed three times with PBS using a BioTek EL406 plate washer, and a TECAN Freedom Evo 150 transferred 100 μ L of inhibitor-containing media to each well. Cells were incubated at

37 °C, 5% CO₂ for 1 h, and then the TECAN was used to transfer 5 μL of nanoparticle solution to each well. The cells were incubated with nanoparticles for 4 h, and then the BioTek plate washer was used to wash the plates three times with PBS and to add 20 μL of trypsin EDTA to each well. After a 5 min incubation at 37 °C, 5% CO₂, 80 μL of complete media supplemented with propidium iodide was added to each well. The live cells were then analyzed using a BD LSR2 cytometer.

For the 24 h cholesterol depletion experiment, cells were seeded at the same density and allowed to adhere for 24 h. The cells were then treated with nanoparticles in the same way as above, but incubated for 24 h. After 24 h, the cells were washed three times with PBS, and 100 μL of methyl-beta cyclodextrin-containing media was added to each well. The cells were incubated for 4 h and then washed three times with PBS and processed as described above for analysis by flow cytometry. All data were analyzed using FlowJo software, where live single-cell populations were quantified for nanoparticle-associated fluorescence. Fluorescence quantification was exported for visualization and statistical analysis on GraphPad PRISM.

Patient-Derived Xenograft Experiments. Patient-derived xenograft cell lines were grown orthotopically (intraperitoneal injection) in NSG mice (6–8 weeks old, Jackson Laboratories) and were viably banked for *in vitro* experiments, as described previously.³⁶ PDX cells were cultured *in vitro* in a ovarian cancer primary culture media³⁷ seeded at 500 000 cells per well in low-bind 96-well plates and treated with NPs for 24 h. Samples of the PDX spheroid suspension were used for microscopy and flow cytometry. For flow cytometry, the spheroid suspension was pelleted using centrifugation (RCF 300, 5 min) and washed with PBS. PDX spheroids were incubated in 1× TrypLE Express 30 for 10 min. The suspension was then passed 3× through 70 and 40 μm cell strainers and 2× through a FACS filter cap (BD). The samples were analyzed using a BD LSR2 cytometer to detect mCherry signal and green-fluorescent nanoparticle signal. Cells were engineered to express cytoplasmic mCherry as described previously.³⁶

For confocal microscopy of the PDX spheroids, the samples isolated prior to flow analysis were pelleted in FACS tubes (300 RCF, 5 min). The cells were resuspended in 300 μL of PBS, and then 100 μL of 16% methanol-free formaldehyde (Pierce) was added under agitation. The cells were fixed at room temperature for 10 min, then washed *via* centrifugation and resuspended in 300 μL of PBS. The spheroid suspension was then added to chambered coverslips and imaged directly using an Olympus FV1200, as described in the fixed cell imaging methods above.

Animal Studies. All animal experiments were approved by the Massachusetts Institute of Technology Committee on Animal Care (CAC) and were conducted under the oversight of the Division of Comparative Medicine (DCM).

Biodistribution Studies. Female NCR nude sp/sp mice were purchased from Taconic and kept on an AIN-93 imaging diet for at least 1 week prior to biodistribution experiments. Mice were injected intraperitoneally with 100 000 OVCAR8 mCherry/luciferase cells in PBS and allowed to develop metastatic disease over the course of 4–8 weeks. Mice were randomly assigned to a nanoparticle treatment and were then dosed with 8.3×10^{12} nanoparticles/kg formulated in 5% dextrose in Milli-Q water. All nanoparticles prepared for animal experiments were generated from infrared fluorescent CML cores (ThermoFisher). Dosing was performed either systemically (by retro-orbital injection or tail-vein injection) or intraperitoneally *via* an IP injection. Mice were sacrificed at 24, 48, and 72 h depending on the randomly assigned time point. Immediately following, full necropsies were performed to harvest tumors, lungs, heart, spleen, liver, intestines, kidneys, and stomach from each mouse. The organs were immersed in 12-well plates containing 300 μg/mL D-luciferin PBS solution. The organs were allowed to incubate for at least 15 min in the D-luciferin solution prior to imaging on a Xenogen IVIS Imaging System (PerkinElmer). Organs were imaged using the bioluminescence imaging functionality to identify signal from OVCAR8 cells in the primary tumor masses and from metastatic nodules that could not be removed from the other organs. The organs were also imaged to detect nanoparticle signal using the fluorescence imaging function, using a 710 excitation and 760 emission filter. After imaging, all organs were placed

into tared tubes and weighed to record organ masses into Excel spreadsheets. IVIS data were analyzed using the LivingImage software, where total radiant efficiency (TRE) for each organ was measured and exported to Excel spreadsheets. A python script was then used to extract the data from spreadsheets and sort it into a database for subsequent processing. Nanoparticle signal was baseline-corrected using the values measured for empty wells, and then a total recovered fluorescence value was generated from the sum of the total radiant efficiency (STRE) measured for each organ of a given mouse. The TRE of each organ was normalized by the STRE to generate a % recovered fluorescence value (%RFV) for each organ. The %RFV was then normalized to organ mass in grams to generate the final metric used to quantify biodistribution. The processed data were then exported to GraphPad PRISM for additional statistical analysis.

After imaging and weighing all the organs from the biodistribution studies, the tissues were transferred to 10% formalin for 72 h. Afterward, the tissues were rinsed thoroughly in Milli-Q water and then transferred to 70% ethanol for long-term storage. Some of the tumor tissues were used for histology and for whole-tissue imaging described below.

Histology and Immunofluorescence. The fixed tissue (prepared as described above) was taken and sucrose-infiltrated by immersion in 15% sucrose Milli-Q water for 4 h at 4 °C. Tissues were then transferred to 30% sucrose solutions and held overnight at 4 °C. Next, the tissues were blotted dry using Kimwipes and washed three times using OCT medium. Finally, the tissue was cryomolded in OCT using a snap-freezing method. Briefly, cryomolds were placed on a Petri dish floating over liquid nitrogen for 10 min or until the top of the OCT mold became opaque. The molds were maintained at –80 °C until they could be cryosectioned by the Koch Institute's histology core facility. Afterward, the samples were stained with DAPI and coverslipped using Vectashield mountant. The slides were then imaged using a Panoramic fluorescent slide scanner, using the DAPI, TRITC, and Cy7 channels to detect nuclei, mCherry, and nanoparticle signal, respectively. Detailed images were obtained using an FV1200 laser scanning confocal microscope.

Multiphoton Imaging of Whole Tissues. Fixed whole tumor tissue was imaged using an Olympus FV1000 multiphoton laser scanning confocal microscope. The 25×, 1.05 NA objective was used to image two tumor z-stacks for each mouse analyzed, following 10 μm steps. The 690–1040 nm laser was used at 710 to excite the nanoparticle, and regular fluorescence data were acquired in the red filter (572–642 nm) due to the broad emission spectrum from the fluorescent core. Multiphoton events from the nanoparticle were captured by the UV filter (410–440 nm). The laser was then set to 840 nm to capture the second harmonic from tissue collagen and to obtain two-photon event data from the mCherry expressed by OVCAR8 cells. To quantify the data, the deepest tissue penetration observed for each z-stack was averaged together for each treatment condition.

Co-localization Analysis of Super-resolution Images. Source images were imported into FIJI as a 32-bit hyperstack, where they were normalized based on background and maximum values measured from the maximum intensity projection. Channels were separated into dedicated stacks and converted to 16-bit images. Built-in functionalities in FIJI were used to threshold the channels and calculate an image of overlapping pixels. Pixels in the thresholded channels and overlap image were counted to determine the fraction of co-localized pixels.

Statistical Analysis. GraphPad PRISM was used to perform statistical analyses. Multiple comparisons were performed using multiple *t* tests, one-way ANOVA, or two-way ANOVA followed by the two-stage step-up false discovery rate method of Benjamini, Krieger, and Yekutieli,³⁸ with *Q* set to 5%.

Data Availability. The data for this study are available within the article, with additional data available in the [Supporting Information](#). Raw data are available upon reasonable request from the corresponding author.

ASSOCIATED CONTENT

SI Supporting Information

The Supporting Information is available free of charge at <https://pubs.acs.org/doi/10.1021/acsnano.9b09213>.

Additional supporting figures of TEM, fluorescence microscopy, and whole-animal imaging (PDF)

AUTHOR INFORMATION

Corresponding Author

Paula T. Hammond – Koch Institute for Integrative Cancer Research, Department of Chemical Engineering, and Institute for Soldier Nanotechnologies, Massachusetts Institute of Technology, Cambridge, Massachusetts 02142, United States; orcid.org/0000-0002-9835-192X; Email: hammond@mit.edu

Authors

Santiago Correa – Department of Biological Engineering, Massachusetts Institute of Technology, Cambridge, Massachusetts 02142, United States

Natalie Boehnke – Koch Institute for Integrative Cancer Research, Massachusetts Institute of Technology, Cambridge, Massachusetts 02142, United States; orcid.org/0000-0002-3468-2033

Antonio E. Barberio – Department of Chemical Engineering, Massachusetts Institute of Technology, Cambridge, Massachusetts 02142, United States

Elad Deiss-Yehiely – Department of Materials Science and Engineering, Massachusetts Institute of Technology, Cambridge, Massachusetts 02142, United States; orcid.org/0000-0002-4345-7903

Aria Shi – Department of Biological Engineering, Massachusetts Institute of Technology, Cambridge, Massachusetts 02142, United States; orcid.org/0000-0002-0695-7124

Benjamin Oberlton – Department of Biological Engineering, Massachusetts Institute of Technology, Cambridge, Massachusetts 02142, United States

Sean G. Smith – Koch Institute for Integrative Cancer Research and Department of Chemical Engineering, Massachusetts Institute of Technology, Cambridge, Massachusetts 02142, United States

Ioannis Zervantonakis – Department of Cell Biology, Ludwig Center at Harvard, Harvard Medical School, Boston, Massachusetts 02115, United States

Erik C. Dreaden – Koch Institute for Integrative Cancer Research, Massachusetts Institute of Technology, Cambridge, Massachusetts 02142, United States

Complete contact information is available at:

<https://pubs.acs.org/doi/10.1021/acsnano.9b09213>

Author Contributions

S.C. and P.T.H. designed the experiments, analyzed the data, and wrote the paper. S.C., N.B., A.E.B., E.D.Y., A.S., B.J.O., S.G.O., I.K.Z., and E.C.D. conducted experiments. S.C. carried out statistical analysis and data visualization. N.B., E.C.D., and I.K.Z. provided advice and technical support throughout. P.T.H. supervised the study. All authors contributed to interpretation of the results and preparation of the paper.

Notes

The authors declare no competing financial interest.

ACKNOWLEDGMENTS

This work was supported by the U.S. Department of Defense Congressionally Directed Medical Research Programs (P.T.H., Teal Innovator Award W81XWH-13-1-0151), the Ovarian

Cancer Research Fund (P.T.H., Collaborative Research Development Grant), the National Institutes of Health (E.C.D., NIBIB 1F32EB017614), the Koch Institute's Marble Center for Cancer Nanomedicine Fellowship (N.B., S.G.S.), the Sloan UCEM Fellowship (S.C.), the Siebel Scholars Fellowship (S.C.), and the National Science Foundation (S.C., G.F.R.P. 1122374). Resources were provided in part by the Koch Institute Support Grant (P30-CA14051) from the National Cancer Institute and the MIT MRSEC Shared Experimental Facilities Grant (DMR-0819762) from the National Science Foundation. The authors would like to thank the MIT Koch Institute Swanson Biotechnology Center, which is supported by the Koch Institute Core Grant P30-CA14051 from the NCI. More specifically, we thank Jaime H. Cheah and Christian K. Soule in the High Throughput Screening Facility, Glenn Paradis in the Flow Cytometry Facility, Jeffrey Wyckoff, Eliza Vasile, and Jeffrey Kuhn in the Microscopy Core, and Kathleen S. Cormier in the Tang Histology Facility. We thank Joan S. Brugge for helpful discussion and facilitating access to patient-derived cells. The authors also thank Kelly D. Moynihan for helpful discussion on multicolor flow analysis, Jiahe Le for facilitating access to fluorescent reporter cell lines, and Shawn A. Musgrave for helpful discussion and advice.

REFERENCES

- (1) Nel, A. E.; Madler, L.; Velegol, D.; Xia, T.; Hoek, E. M.; Somasundaran, P.; Klaessig, F.; Castranova, V.; Thompson, M. Understanding Biophysicochemical Interactions at the Nano-Bio Interface. *Nat. Mater.* **2009**, *8*, 543–557.
- (2) Walkey, C. D.; Olsen, J. B.; Guo, H.; Emili, A.; Chan, W. C. Nanoparticle Size and Surface Chemistry Determine Serum Protein Adsorption and Macrophage Uptake. *J. Am. Chem. Soc.* **2012**, *134*, 2139–2147.
- (3) Bertrand, N.; Grenier, P.; Mahmoudi, M.; Lima, E. M.; Appel, E. A.; Dormont, F.; Lim, J. M.; Karnik, R.; Langer, R.; Farokhzad, O. C. Mechanistic Understanding of *In Vivo* Protein Corona Formation on Polymeric Nanoparticles and Impact on Pharmacokinetics. *Nat. Commun.* **2017**, *8*, 777.
- (4) Perrault, S. D.; Walkey, C.; Jennings, T.; Fischer, H. C.; Chan, W. C. Mediating Tumor Targeting Efficiency of Nanoparticles Through Design. *Nano Lett.* **2009**, *9*, 1909–1915.
- (5) Dai, Q.; Walkey, C.; Chan, W. C. Polyethylene Glycol Backfilling Mitigates the Negative Impact of the Protein Corona on Nanoparticle Cell Targeting. *Angew. Chem., Int. Ed.* **2014**, *53*, 5093–5096.
- (6) Matsumura, Y.; Maeda, H. A New Concept for Macromolecular Therapeutics in Cancer Chemotherapy: Mechanism of Tumoritropic Accumulation of Proteins and the Antitumor Agent Smancs. *Cancer Res.* **1986**, *46*, 6387–6392.
- (7) Maeda, H.; Wu, J.; Sawa, T.; Matsumura, Y.; Hori, K. Tumor Vascular Permeability and the EPR Effect in Macromolecular Therapeutics: a Review. *J. Controlled Release* **2000**, *65*, 271–284.
- (8) Jain, R. K.; Stylianopoulos, T. Delivering Nanomedicine to Solid Tumors. *Nat. Rev. Clin. Oncol.* **2010**, *7*, 653–664.
- (9) Chen, H.; Zhang, W.; Zhu, G.; Xie, J.; Chen, X. Rethinking Cancer Nanotheranostics. *Nat. Rev. Mater.* **2017**, *2*, 17024.
- (10) Verma, A.; Stellacci, F. Effect of Surface Properties on Nanoparticle-Cell Interactions. *Small* **2010**, *6*, 12–21.
- (11) Wilhelm, S.; Tavares, A. J.; Dai, Q.; Ohta, S.; Audet, J.; Dvorak, H. F.; Chan, W. C. W. Analysis of Nanoparticle Delivery to Tumours. *Nat. Rev. Mater.* **2016**, *1*, 16014.
- (12) Caruso, F.; Lichtenfeld, H.; Giersig, M.; Mohwald, H. Electrostatic Self-Assembly of Silica Nanoparticle - Polyelectrolyte Multilayers on Polystyrene Latex Particles. *J. Am. Chem. Soc.* **1998**, *120*, 8523–8524.

- (13) Wang, Y.; Angelatos, A. S.; Caruso, F. Template Synthesis of Nanostructured Materials via Layer-by-Layer Assembly. *Chem. Mater.* **2008**, *20*, 848–858.
- (14) Hammond, P. T. Polyelectrolyte Multilayered Nanoparticles: Using Nanolayers for Noncontrolled and Targeted Systemic Release. *Nanomedicine (London, U. K.)* **2012**, *7*, 619–622.
- (15) Correa, S.; Boehnke, N.; Deiss-Yehiely, E.; Hammond, P. T. Solution Conditions Tune and Optimize Loading of Therapeutic Polyelectrolytes into Layer-by-Layer Functionalized Liposomes. *ACS Nano* **2019**, *13*, 5623–5634.
- (16) Correa, S.; Choi, K. Y.; Dreaden, E. C.; Renggli, K.; Shi, A.; Gu, L.; Shopsowitz, K. E.; Quadir, M. A.; Ben-Akiva, E.; Hammond, P. T. Highly Scalable, Closed-Loop Synthesis of Drug-Loaded, Layer-by-Layer Nanoparticles. *Adv. Funct. Mater.* **2016**, *26*, 991–1003.
- (17) Lengyel, E. Ovarian Cancer Development and Metastasis. *Am. J. Pathol.* **2010**, *177*, 1053–1064.
- (18) Tarin, D.; Price, J. E.; Kettlewell, M. G. W.; Souter, R. G.; Vass, A. C. R.; Crossley, B. Mechanisms of Human Tumor Metastasis Studied in Patients with Peritoneovenous Shunts. *Cancer Res.* **1984**, *44*, 3584–3592.
- (19) Goodman, C. M.; McCusker, C. D.; Yilmaz, T.; Rotello, V. M. Toxicity of Gold Nanoparticles Functionalized with Cationic and Anionic Side Chains. *Bioconjugate Chem.* **2004**, *15*, 897–900.
- (20) Frohlich, E. The Role of Surface Charge in Cellular Uptake and Cytotoxicity of Medical Nanoparticles. *Int. J. Nanomed.* **2012**, *7*, 5577–5591.
- (21) Dreaden, E. C.; Morton, S. W.; Shopsowitz, K. E.; Choi, J. H.; Deng, Z. J.; Cho, N. J.; Hammond, P. T. Bimodal Tumor-Targeting from Microenvironment Responsive Hyaluronan Layer-by-Layer (LbL) Nanoparticles. *ACS Nano* **2014**, *8*, 8374–8382.
- (22) Tsutsui, J.; Kadomatsu, K.; Matsubara, S.; Nakagawara, A.; Hamanoue, M.; Takao, S.; Shimazu, H.; Ohji, Y.; Muramatsu, T. A New Family of Heparin-Binding Growth/Differentiation Factors: Increased Midkine Expression in Wilms' Tumor and Other Human Carcinomas. *Cancer Res.* **1993**, *53*, 1281–1285.
- (23) van Dam, G. M.; Themelis, G.; Crane, L. M.; Harlaar, N. J.; Pleijhuis, R. G.; Kelder, W.; Sarantopoulos, A.; de Jong, J. S.; Arts, H. J.; van der Zee, A. G.; Bart, J.; Low, P. S.; Ntziachristos, V. Intraoperative Tumor-Specific Fluorescence Imaging in Ovarian Cancer by Folate Receptor-Alpha Targeting: First In-Human Results. *Nat. Med.* **2011**, *17*, 1315–1319.
- (24) Patel, M. M.; Smart, J. D.; Nevell, T. G.; Ewen, R. J.; Eaton, P. J.; Tsibouklis, J. Mucin/Poly(Acrylic Acid) Interactions: A Spectroscopic Investigation of Mucoadhesion. *Biomacromolecules* **2003**, *4*, 1184–1190.
- (25) Solomonidou, D.; Cremer, K.; Krumme, M.; Kreuter, J. Effect of Carbomer Concentration and Degree of Neutralization on the Mucoadhesive Properties of Polymer Films. *J. Biomater. Sci., Polym. Ed.* **2001**, *12*, 1191–1205.
- (26) Chauhan, S. C.; Kumar, D.; Jaggi, M. Mucins in Ovarian Cancer Diagnosis and Therapy. *J. Ovarian Res.* **2009**, *2*, 21.
- (27) Tarhriz, V.; Bandehpour, M.; Dastmalchi, S.; Ouladsahebmadarek, E.; Zarredar, H.; Eyvazi, S. Overview of CD24 as a New Molecular Marker in Ovarian Cancer. *J. Cell. Physiol.* **2019**, *234*, 2134–2142.
- (28) Staubach, S.; Hanisch, F. G. Lipid Rafts: Signaling and Sorting Platforms of Cells and their Roles in Cancer. *Expert Rev. Proteomics* **2011**, *8*, 263–277.
- (29) Staubach, S.; Razawi, H.; Hanisch, F. G. Proteomics of MUC1-Containing Lipid Rafts from Plasma Membranes and Exosomes of Human Breast Carcinoma Cells MCF-7. *Proteomics* **2009**, *9*, 2820–2835.
- (30) Wright, A. A.; Cronin, A.; Milne, D. E.; Bookman, M. A.; Burger, R. A.; Cohn, D. E.; Cristea, M. C.; Griggs, J. J.; Keating, N. L.; Levenback, C. F.; Mantia-Smaldone, G.; Matulonis, U. A.; Meyer, L. A.; Niland, J. C.; Weeks, J. C.; O'Malley, D. M. Use and Effectiveness of Intraperitoneal Chemotherapy for Treatment of Ovarian Cancer. *J. Clin. Oncol.* **2015**, *33*, 2841–2847.
- (31) Markman, M.; Bundy, B. N.; Alberts, D. S.; Fowler, J. M.; Clark-Pearson, D. L.; Carson, L. F.; Wadler, S.; SICKEL, J. Phase III Trial of Standard-Dose Intravenous Cisplatin Plus Paclitaxel versus Moderately High-Dose Carboplatin Followed by Intravenous Paclitaxel and Intraperitoneal Cisplatin in Small-Volume Stage III Ovarian Carcinoma: An Intergroup Study of the Gynecologic Oncology Group, Southwestern Oncology Group, and Eastern Cooperative Oncology Group. *J. Clin. Oncol.* **2001**, *19*, 1001–1007.
- (32) Alberts, D. S.; Liu, P. Y.; Hannigan, E. V.; O'Toole, R.; Williams, S. D.; Young, J. A.; Franklin, E. W.; Clarke-Pearson, D. L.; Malviya, V. K.; DuBeshter, B. Intraperitoneal Cisplatin plus Intravenous Cyclophosphamide versus Intravenous Cisplatin plus Intravenous Cyclophosphamide for Stage III Ovarian Cancer. *N. Engl. J. Med.* **1996**, *335*, 1950–1955.
- (33) Bajaj, G.; Yeo, Y. Drug Delivery Systems for Intraperitoneal Therapy. *Pharm. Res.* **2010**, *27*, 735–738.
- (34) Deng, Y.; Yang, F.; Cocco, E.; Song, E.; Zhang, J.; Cui, J.; Mohideen, M.; Bellone, S.; Santin, A. D.; Saltzman, W. M. Improved I.P., Drug Delivery with Bioadhesive Nanoparticles. *Proc. Natl. Acad. Sci. U. S. A.* **2016**, *113*, 11453–11458.
- (35) Bu, P.; Chen, K.-Y.; Xiang, K.; Johnson, C.; Crown, S. B.; Rakhilin, N.; Ai, Y.; Wang, L.; Xi, R.; Astapova, I.; Han, Y.; Li, J.; Barth, B. B.; Lu, M.; Gao, Z.; Mines, R.; Zhang, L.; Herman, M.; Hsu, D.; Zhang, G.-F.; Shen, X. Aldolase B-Mediated Fructose Metabolism Drives Metabolic Reprogramming of Colon Cancer Liver Metastasis. *Cell Metab.* **2018**, *27*, 1249–1262.
- (36) Liu, J. F.; Palakurthi, S.; Zeng, Q.; Zhou, S.; Ivanova, E.; Huang, W.; Zervantonakis, I. K.; Selfors, L. M.; Shen, Y.; Pritchard, C. C.; Zheng, M.; Adleff, V.; Papp, E.; Piao, H.; Novak, M.; Fotheringham, S.; Wulf, G. M.; English, J.; Kirschmeier, P. T.; Velculescu, V. E.; Paweletz, C.; Mills, G. B.; Livingston, D. M.; Brugge, J. S.; Matulonis, U. A.; Drapkin, R. Establishment of Patient-Derived Tumor Xenograft Models of Epithelial Ovarian Cancer for Preclinical Evaluation of Novel Therapeutics. *Clin. Cancer Res.* **2017**, *23*, 1263–1273.
- (37) Zervantonakis, I. K.; Iavarone, C.; Chen, H.-Y.; Selfors, L. M.; Palakurthi, S.; Liu, J. F.; Drapkin, R.; Matulonis, U.; Levenson, J. D.; Sampath, D.; Mills, G. B.; Brugge, J. S. Systems Analysis of Apoptotic Priming in Ovarian Cancer Identifies Vulnerabilities and Predictors of Drug Response. *Nat. Commun.* **2017**, *8*, 365.
- (38) Glickman, M. E.; Rao, S. R.; Schultz, M. R. False Discovery Rate Control is a Recommended Alternative to Bonferroni-Type Adjustments in Health Studies. *J. Clin. Epidemiol.* **2014**, *67*, 850–857.